

Peptide-Modified Dendrimers as Templates for the Production of Highly Reactive Catalytic Nanomaterials

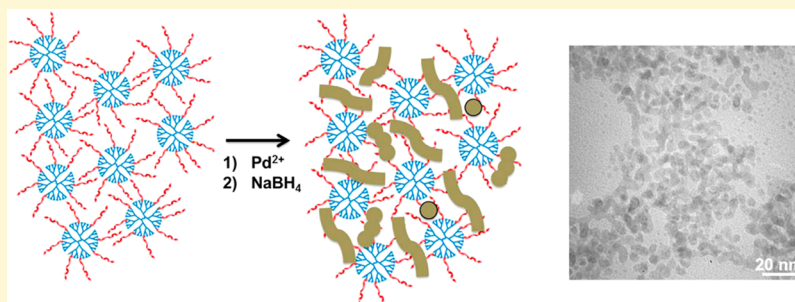
Nicholas M. Bedford,^{†,‡} Rohit Bhandari,^{‡,||} Joseph M. Slocik,[†] Soenke Seifert,[§] Rajesh R. Naik,^{*,†} and Marc R. Knecht^{*,‡}

[†]Materials and Manufacturing Directorate, Air Force Research Laboratory, Wright-Patterson Air Force Base, Ohio 45433, United States

[‡]Department of Chemistry, University of Miami, 1301 Memorial Drive, Coral Gables, Florida 33146, United States

[§]X-ray Science Division, Argonne National Laboratory, 9700 South Cass Avenue, Argonne, Illinois 60439, United States

S Supporting Information



ABSTRACT: Peptide-driven nanomaterials synthesis and assembly has become a significant research thrust due to the capability to generate a range of multifunctional materials with high spatial precision and tunable properties. Despite the extensive amount of available literature, the majority of studies report the use of free peptides to drive synthesis and assembly. Such strategies are not an entirely accurate representation of nature, as many materials binding peptides found in biological systems are sterically constrained to a larger biological motif. Herein we report the synthesis of catalytic Pd nanomaterials using constrained peptides covalently attached to the surface of small, water-soluble dendrimers. Using the R5 peptide conjugated to polyamidoamine dendrimer as a bioconjugate, Pd nanomaterials were generated that displayed altered morphologies compared to nanomaterials templated with free R5. It was discovered that the peptide surface density on the dendrimer affected the resulting nanoscale morphology. Furthermore, the catalytic activities of Pd materials templated with R5/dendrimer are higher as compared to the R5-templated Pd materials for the hydrogenation of allyl alcohol, with an average increase in turnover frequency of ~ 1500 mol product $(\text{mol Pd} \times \text{h})^{-1}$. Small angle X-ray scattering analysis and dynamic light scattering indicate that Pd derived from R5/dendrimer templates remained less aggregated in solution and displayed more available reactive Pd surface area. Such morphological changes in solution are attributed to the constrained peptide binding motifs, which altered the Pd morphology and subsequent properties. Moreover, the results of this study suggest that constrained materials binding peptide systems can be employed as a means to alter morphology and improve resulting properties.

INTRODUCTION

Peptide-driven fabrication methods represent an emerging direction for the ambient synthesis and assembly of nanostructured materials.^{1–3} Inspired by biomineralization, peptide sequences discovered via biocombinatorial selection techniques or isolated directly from an organism have been found to fabricate a wide variety of nanoscale materials by binding to the inorganic surface. Using these approaches, metal,^{4–8} metal oxide,^{9–13} semiconductor,^{14–17} and carbon^{18–21} nanomaterials have been generated/assembled under energy-friendly and aqueous reaction conditions. These ambient conditions, coupled with inherent biological specificity,²² make peptide-driven nanomaterial production an attractive alternative to traditional routes that require energy-intensive reactions with nonspecific organic ligands to stabilize the structures. This is

especially important considering that the noncovalent interactions of peptide binding could potentially be tailored for additional capabilities that are not possible using covalently bound ligands. Furthermore, the ability to form multifunctional structures via fusion peptides can also be achieved by incorporating two material binding domains into a single sequence.^{23–25} Such ligand programmability and material structural control ultimately allows for the fine-tuning of emergent properties. Taken together, these biomimetic materials possess important and tunable properties that could

Received: March 1, 2014

Revised: June 16, 2014

Published: July 8, 2014

be exploited for optical,^{17,26} energy harvesting/storage,^{27,28} sensing,^{29,30} and catalytic^{31,32} applications.

Materials binding sequences are commonly used as free peptides in solution to generate nanostructures by binding to the surface of the growing inorganic component.^{5–7} While this can produce the desired materials, such flexibility is quite different than that of the peptide morphology found in nature where the N- and/or C-termini of the sequence are typically attached to a larger protein construct.^{12,33} This subtlety could possess significant implications over nanomaterial synthesis and assembly. For instance, sequences isolated from biomineralizing species are commonly derived from membrane bound proteins,^{12,33} while peptides discovered via biopanning techniques, such as phage and cell-surface display, are anchored onto the surface of the panning moiety.² Previous work by the Belcher group has demonstrated that constraining such material binding sequences along virus backbones can be employed to template inorganic structures, resulting in the production of anisotropic nanowires.^{16,24,27} These structures have important catalytic and energy harvesting capabilities that exploit the one-dimensional nature of the virus. Furthermore, Rosi and colleagues have used hybrid DNA-modified peptides that self-assemble to generate helical nanoribbons of Au nanoparticles.³⁴ This process provides enhanced control over both the global and local assembly construct via incorporation of the peptide into a supramolecular framework, where the biomolecule retains its ability to recognize and bind Au nanoparticles.

In contrast, certain materials binding peptides can assemble into larger macromolecular aggregates in solution depending on the location of the amino acids in the primary sequence. One example is the R5 peptide (SSKKSGSYSGKSKRRIL), derived from the biosilica producing diatom *Cylindrotheca fusiformis*.³³ The presence of the RRIL motif at the C-terminal region of the largely hydrophilic sequence likely drives peptide aggregate formation, wherein the RRIL component is buried within the core of the framework to display the highly polar functionalities to solution. This architecture allows the peptide to be exploited as a template for other nonsilica nanomaterials as well.^{35–40} One such example is the formation of catalytic Pd nanomaterials, where previously a dependence upon the Pd:R5 ratio over the final morphology of the encapsulated metallic component was demonstrated.^{38–41} Using this sequence, the morphologies of Pd nanomaterials ranged from spherical nanoparticles at low ratios to linear nanoribbons and branching nanoparticle networks (NPNs) at higher ratios.^{38–40} These structures have been shown to be highly reactive in catalytic C–C coupling, 4-nitrophenol reduction, and olefin hydrogenation reactions.^{38–40}

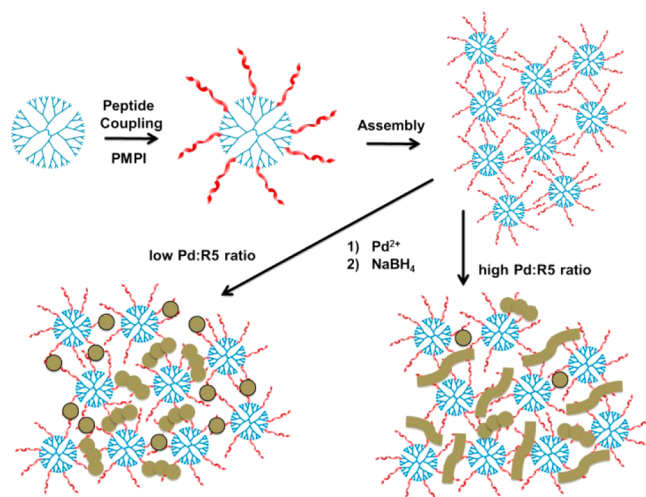
In this contribution, we report the use of R5-dendrimer conjugates as templates for the fabrication of Pd nanomaterials, where the biotemplate dramatically influences the catalytic activity of the final structures. Dendrimers are monodisperse, spherical polymers radially grown from a central core.⁴² This architecture yields a macromolecular structure of a semihollow interior with tunable surface functionalities for potential applications in nanomaterial production^{43–45} and biomedicine.^{46–48} For this study, hydroxyl-terminated fourth generation polyamidoamine (G4 PAMAM–OH) dendrimers were used as a water-soluble framework to which the R5 peptide was covalently attached, creating a unique biomimetic dendritic scaffold for the templating of inorganic nanomaterials. Using the R5/dendrimer templates, highly reactive Pd nanostructures of multiple morphologies ranging from nanoparticles to NPNs

were produced, which are not observed using the free peptide template. Such morphological diversity is attributed to the confined orientation of the R5 bound to the surface of the dendrimer, where the peptide surface density was noted to impact the overall metallic structure. Once produced, the biotemplated materials were employed as catalysts for the hydrogenation of allyl alcohol, from which the calculated turnover frequency (TOF) values were greatly enhanced compared to the materials generated using the dendrimer-free R5 scaffold. The TOF values were exceedingly high, suggesting that the dendritic template is enhanced for both materials production and catalytic application. To study this effect, the peptide–dendrimer templated Pd nanomaterials were examined using small-angle X-ray scattering (SAXS) and dynamic light scattering (DLS), which demonstrated a more porous macrostructure of the bio/dendrimer template in solution with a higher degree of catalytic surface area for the Pd component as compared to the structures encapsulated by the native R5 template. As a result, these studies suggest that peptide-modified dendrimers represent innovative biomimetic templates where the molecular rigidity and global framework directly affect the catalytic functionality.

RESULTS AND DISCUSSION

Cysteine modified R5 peptides were covalently attached to the surface of hydroxyl terminated G4 PAMAM dendrimers using *N*-(*p*-maleimidophenyl) isocyanate (PMPI), a common hydroxyl-to-thiol coupling agent (Scheme 1). In this reaction, the

Scheme 1. Synthesis of the R5/Dendrimer Template and Subsequent Pd Nanomaterial Generation



hydroxyl groups on the surface of the dendrimer react with the isocyanate groups in PMPI to make the dendrimer suitable for subsequent thiol attachment. Cysteine labeled R5 then couples to the maleimide portion of PMPI to form a thioether linkage, successfully conjugating the peptide to the surface of the dendrimer (see Supporting Information, Scheme S1, for more details). As R5 lacks a native thiol functionality, cysteine was inserted onto the peptide sequence at the N-terminus, thus displaying the RRIL motif to solution to promote self-assembly. Once coupled, the peptide surface density could affect both metal templating and the final nanomaterial morphology; thus, peptide coverage of the dendrimer surface was studied at R5:dendrimer ratios of 4, 8, and 16. The use of G4-PAMAM

(versus smaller dendrimer generations) allows these surface densities to be explored while minimizing steric crowding of the peptide at the dendrimer surface. To differentiate between the various materials prepared, the metallic structures are defined as XR5(PdY), where X represents the number of peptides present on the dendrimer surface (4, 8, or 16) and Y denotes the Pd:peptide ratio employed to prepare the metallic nanostructures. Note that Pd:peptide ratios were used for the fabrication of all of the inorganic materials and not Pd:dendrimer ratios.

Once the biomimetic template was generated, IR spectroscopy was performed on lyophilized material to confirm peptide

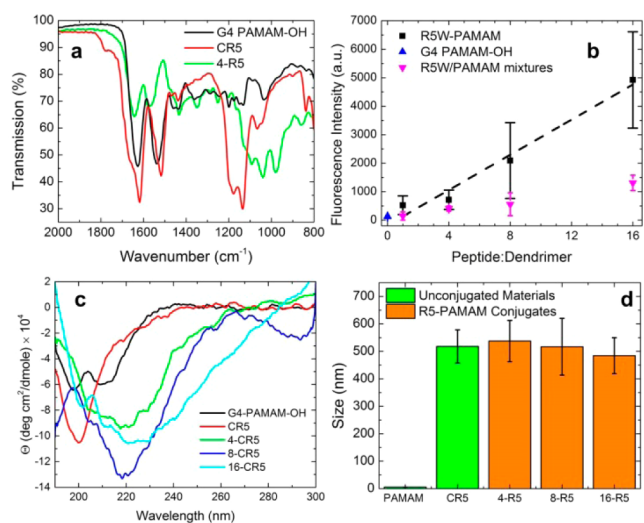


Figure 1. Characterization of the R5/dendrimer conjugate formation, peptide surface density, peptide confirmation, and aggregate size via (a) IR, (b) fluorescence, and (c) CD spectroscopy. Part (d) presents the DLS size analysis of the generated biotemplates.

conjugation to the dendrimer periphery (Figure 1a). The bare dendrimer spectrum (black plot) exhibits peaks at 1624 and 1542 cm^{-1} corresponding to the amide stretches found throughout the repeating, branched polymeric structure. For the free CR5 peptide (red plot), amide peaks are also present at 1618 and 1516 cm^{-1} arising from the amides of the peptide backbone, along with a small peak at 1780 cm^{-1} corresponding to the thiol group of cysteine.⁴⁹ Large absorptions at 1178 and 1134 cm^{-1} are also present for CR5, corresponding to amide III absorption from intra- and intermolecular interaction between amino acid side chains.⁵⁰ Upon conjugation of four equivalents of the CR5 to the dendrimer surface (green plot), the thiol band disappears, concomitant with the production of two new peaks at 1042 and 976 cm^{-1} . These new stretches appear from the generation of the thioether group that conjugates the biomolecules to the polymeric surface.⁵¹ Moreover, the amide III absorptions are also masked, suggesting that the amino acid interactions are substantially changed, likely due to steric hindrance of the peptide, further indicating that the peptides are coupled to the dendrimer surface.

To determine the peptide surface density, a fluorescence assay was conducted wherein tryptophan was used as a fluorescent reporter incorporated at the opposite termini from the cysteine residue (i.e., CR5W). Such a design should allow for the coupling strategy to proceed unimpeded, while allowing for monitoring of the degree of conjugation. After peptide coupling to the dendrimer, the system was dialyzed to remove excess free peptide, and thus any fluorescence signal

can only arise from the biomolecules bound to the dendrimer periphery. As shown in the black plot of Figure 1b, when the CR5W peptide was conjugated to the dendrimer surface, an increase in the fluorescence intensity was observed proportional to the calculated peptide surface density. This result indicates that the peptide–dendrimer conjugates were achieved at the approximate surface densities anticipated based upon the reaction stoichiometry. Note that all of the conjugates have significantly higher fluorescence intensities than the unmodified dendrimer. Moreover, simply mixing the dendrimer and CR5W together without PMPI results in negligible fluorescence signal after dialysis (magenta plot). While a minor fluorescence signal is noted suggesting nonspecific interactions between the peptide and dendrimer, the intensity is much weaker than the values observed with the chemically conjugated biotemplates. This result, along with IR analysis and TEM studies (discussed below), suggested that PMPI-based coupling strategies effectively conjugated the peptide to the dendrimer to form the biomacromolecular structures.

Circular dichroism (CD) spectroscopy was used to probe the conformational changes of the R5 peptide covalently attached to the PAMAM surface. As shown in Figure 1c, the native CR5 peptide (red line) demonstrates a large negative peak at 200 nm, indicative of a random coiled structure. This structure is consistent with previous CD studies of the parent R5⁵² and other short linear peptides.⁵³ Upon conjugation to the rigid dendrimer, the peptides undergo structural changes as observed by drastic changes in the CD spectra for the 4R5, 8R5, and 16R5 species. A very broad peak centered ~ 215 nm is found for the 4R5 sample (green plot), suggesting that the peptide is becoming more structured. This feature was also found in the 8R5 and 16R5 samples (blue and cyan plots, respectively), becoming broader and/or shifting to higher wavelengths. These shifts signify a structural transition from random coil to more helical structures, suggesting that a more compact and constrained orientation of the R5 sequence upon conjugation to the dendrimer periphery. For reference, a spectrum of the PAMAM dendrimer is also shown in Figure 1c, indicating that the features found in the peptide–dendrimer conjugates arise from the peptide only and not from the polymeric core. Such results were anticipated based upon similar peptide structural effects when bound to larger constructs, such as those observed for the variable peptide region when integrated into the phage viral structure.⁵⁴

Deconvolution of the CD spectra assisted in further characterization of the secondary structure of the peptides (Supporting Information, Table S1). The helical content of the unconstrained linear CR5 peptide was minimal, as expected. Upon conjunction of CR5 to the dendrimer, the helical content increases linearly with peptide surface density. This increase in helical nature is also characteristic of other peptide-containing dendrimers.^{55,56} Similarly, the extent of unordered content decreases with increasing peptide density, with the unconstrained CR5 peptide exhibiting the highest percentage of this confirmation. Together, this analysis demonstrates that the R5 peptide is becoming more conformationally hindered at higher surface conjugation ratios due to close proximity of the peptide chains attached to the surface of dendritic core.

DLS was used to probe the aggregate size of the free dendrimer and peptides, as well as the dendrimer/peptide constructs in solution. As shown in Figure 1d, the G4 PAMAM dendrimer displayed an aggregate size of 5.6 ± 0.2 nm, consistent with previously measured dimensions for the

monodisperse structure.⁵⁷ When studying the CR5 peptides, an aggregate size of 520 ± 60 nm was obtained. For reference, under the same conditions, the native R5 that lacks the cysteine residue of the present sequence displayed an aggregate size of 960 ± 43 nm,³⁷ suggesting that the positioning of the thiol group modulated the self-assembly process. Peptide aggregation is anticipated to originate from the RRIL motif, burying this component into a hydrophobic core to expose the hydrophilic residues.⁵⁸ In the CR5, a modestly hydrophobic cysteine is located on the N-terminus, opposite of the RRIL component, thus slightly perturbing the assembly effects in the native peptide, resulting in the observed smaller aggregate size. Once the peptides were conjugated to the dendrimer, an interesting assembly pattern was observed (Figure 1d). For the R5-based conjugates, the sizes varied over a narrow range of 480 ± 70 nm for the 16R5 species until a value of 540 ± 80 nm for the 4R5 conjugate. Such sizes were nearly identical to that of the free CR5 in solution, suggesting that the dendrimer did not significantly inhibit the assembly process. It is interesting to note that despite the potential for extensive cross-linking in the higher surface density conjugates, the size trend, on average, decreases with increasing peptide density. Such results may be due to the effect of the higher peptide surface density leading to sterically restricted biomolecules, thus preventing them from achieving appropriate conformations to drive structural assembly. Note that no free peptide was present in solution due to extensive dialysis, and thus the observed sizes were directly attributed to the peptide/dendrimer conjugates only. Interestingly the sizes obtained for the conjugates are similar to those reported for R5 peptide truncates,⁴¹ suggesting that the assembly process can occur with a constricted RRIL motif but that this portion facilitates the organization event.

Once the peptide/dendrimer scaffolds were confirmed, they were employed for the production of zerovalent Pd nanomaterials. In this regard, Pd²⁺ was incubated with each of the peptide/dendrimer complexes, followed by reduction via NaBH₄. For these materials, the amount of Pd added to each system was determined based upon the number of R5 peptides in the reaction and not the total number of conjugates. From this, a series of Pd:R5 ratios were initially tested for all peptide/dendrimer conjugates, where the upper limit was chosen based on nanomaterial stability. Previous reports using the free R5 peptide have suggested that the ratio of Pd:R5 employed altered the morphology of the templated Pd nanomaterials; at a Pd:R5 ratio of 60 (termed Pd60), spherical nanomaterials were obtained, while for materials prepared at ratios of 90 (Pd90) and 120 (Pd120), anisotropic nanoribbons and NPN morphologies were generated, respectively, due to increased loading of Pd in the template.^{38–40} To this end, as the loading increases, the number of individual nanoparticles increases, resulting in a controlled particle aggregate to form the linear structures within the templates. Such effects are likely to be attenuated by the bulky dendrimers conjugated into the biotemplate, which was fully examined.

Using the series of conjugates prepared, the Pd nanomaterials were generated and analyzed using transmission electron microscopy (TEM). The morphology of the resulting metallic structures depended upon the Pd:peptide ratio, where spherical nanoparticles, as well as linear nanoribbons and NPNs were generated. Particle size and morphology information for all of the stable structures produced using the different templates are summarized in Table 1. Using the 16R5 templates, stable Pd nanomaterials were synthesized at Pd:R5 ratios of 10, 30, and

Table 1. Summary of TEM and Catalytic Observations for the Pd Nanomaterials Templated with the R5–Dendrimer Conjugates

peptide coverage- (Pd amount)	morphology ^a	size (nm)	TOF
			mol product (mol Pd × h) ⁻¹
16R5(Pd10)	particles	2.7 ± 0.6	4800 ± 400
16R5(Pd30)	particles (57%)	2.7 ± 0.6	4600 ± 200
	ribbons (43%)	4.0 ± 0.7	
16R5(Pd60)	NPNs	3.9 ± 1.0	4300 ± 200
8R5(Pd30)	particles (83%)	2.6 ± 0.9	4800 ± 200
	ribbons (17%)	3.4 ± 0.8	
8R5(Pd60)	particles (79%)	2.4 ± 0.5	4800 ± 100
	ribbons (21%)	3.1 ± 0.9	
8R5(Pd90)	particles (23%)	3.0 ± 0.6	4500 ± 200
	ribbons (19%)	3.4 ± 0.6	
4R5(Pd60)	NPNs (58%)	4.7 ± 0.9	4100 ± 400
	particles (88%)	2.5 ± 0.5	
4R5(Pd90)	ribbons (12%)	3.4 ± 0.8	4210 ± 90
	particles (80%)	2.6 ± 0.5	
4R5(Pd120)	ribbons (20%)	3.3 ± 1.1	4400 ± 120
	particles (57%)	2.9 ± 0.5	
	NPNs (43%)	4.5 ± 0.8	

^aMorphology populations estimated from at least five different TEM images.

60, as presented in Figure 2a–c. For the 16R5(Pd10) materials, spherical particles were exclusively generated, with an average diameter of 2.7 ± 0.6 nm. Upon increasing the Pd:R5 ratio to 30 for the 16R5(Pd30) sample, a mixture of spherical particles (57%) and nanoribbons (43%) were observed with an average diameter of 2.7 ± 0.6 nm for the nanoparticles and an average width of 4.0 ± 0.7 nm for the nanoribbons. Further increasing the Pd concentration for the 16R5(Pd60) materials, metallic NPNs were the only morphology observed with an average width of 3.9 ± 1.0 nm. This varying morphology over a wide range of Pd:R5 ratios likely arises from template-directing effects, as discussed below.

In a similar fashion, Pd nanomaterials were fabricated using the 8R5 templates (Figure 2d–f) at Pd:R5 ratios of 30, 60, and 90. Note that this is a similar template as to the one discussed above; however, fewer peptides were displayed at the dendrimer periphery. For this system at the two lower Pd:R5 ratios, particles and ribbons were typically observed. In general, 2.6 ± 0.9 nm nanoparticles were the main component of the 8R5(Pd30) sample at 83% of the material population; however, 17% of the sample was in the nanoribbon morphology (width = 3.4 ± 0.8 nm). For the 8R5(Pd60) sample, spherical nanoparticles again were the predominate morphology with interspersed nanoribbons (79% vs 21%, respectively) with average dimensions of 2.4 ± 0.5 nm (nanoparticle diameter) and 3.1 ± 0.9 nm (nanoribbon width). Interestingly, in the 8R5(Pd90) system, a mixture of all three morphologies was

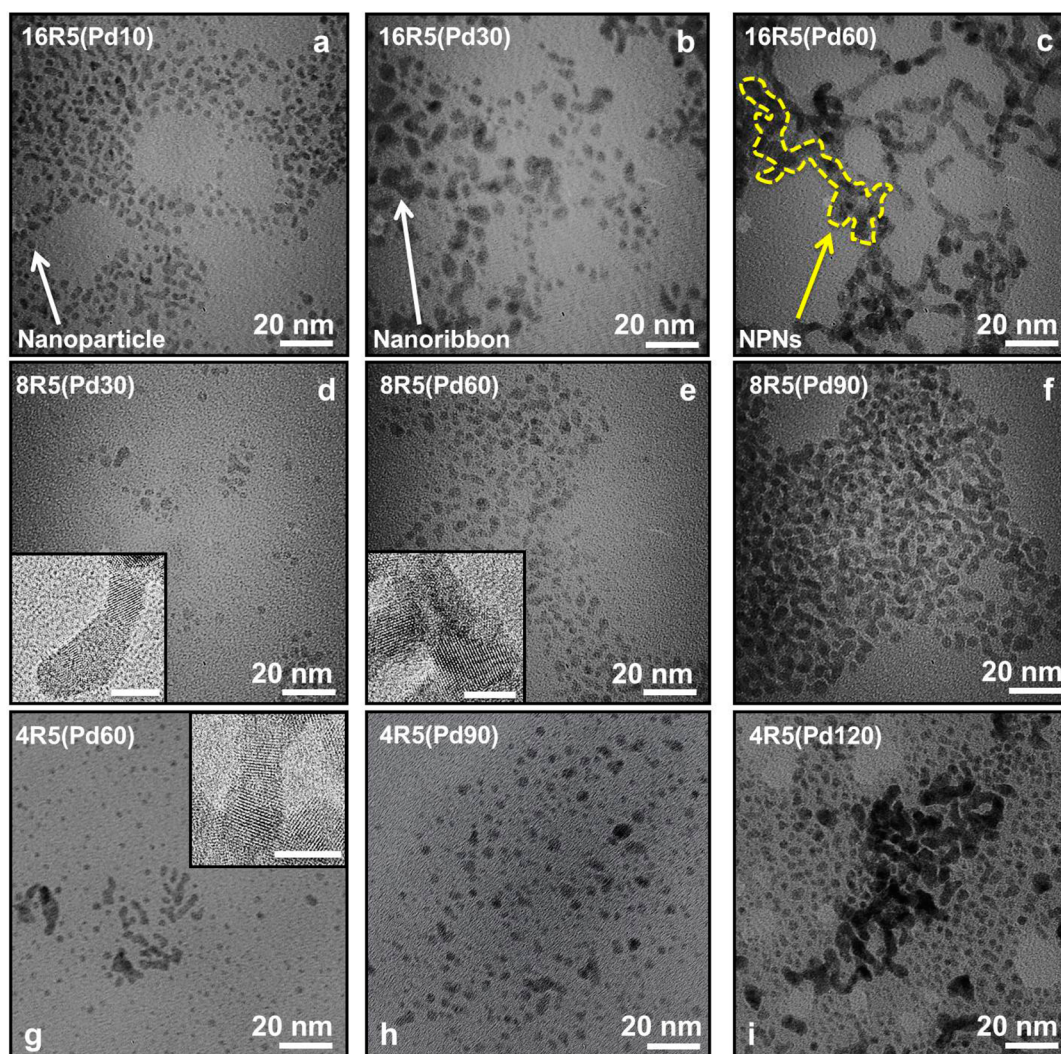


Figure 2. TEM images of Pd nanomaterials templated with (a) 16R5(Pd10), (b) 16R5(Pd30), (c) 16R5(Pd60), (d) 8R5(Pd30), (e) 8R5(Pd60), (f) 8R5(Pd90), (g) 4R5(Pd60), (h) 4R5(Pd90), and (i) 4R5(Pd120). Arrows and outlines in the 16R5 Pd sample show examples of the morphologies discussed in the text. HRTEM images (insets) indicate the presence of Pd lattice fringes for selected samples (8-R5(Pd30), 8-R5(Pd60), and 4-R5(Pd60); inset scale bar = 5 nm).

noted, with NPNs becoming the dominant structure (58%) of an average width of 4.7 ± 0.9 nm. Finally, Pd nanomaterials templated with the 4R5 conjugates also displayed interesting metal loading-dependent morphologies (Figure 2g–i). In this regard, spherical nanoparticles (88%) and nanoribbons (12%) were generated for the 4R5(Pd60) sample (2.5 ± 1.0 nm diameter and 3.4 ± 0.8 nm width, respectively), while at higher ratios, mixtures of nanoparticles, nanoribbons, and NPNs were noted. For instance, spherical nanoparticles (80%, 2.6 ± 0.5 nm) and nanoribbons (20%, 3.3 ± 1.1 nm) were obtained from the 4R5(Pd90) system, while NPNs (43%, 4.5 ± 0.8 nm) and spherical nanoparticles (57%, 2.9 ± 0.5 nm) were found with 4R5(Pd120) template. High-resolution TEM (HRTEM) images for selected samples (insets of Figure 2d,e,g) further confirm the observed morphologies while simultaneously displaying the lattice fringes associated with Pd.

Key morphological differences were observed as compared to the Pd nanomaterials templated by the R5 only scaffold. For example, Pd60 nanomaterials prepared with R5 templates formed spherical particles exclusively,^{38–40} while Pd60 materials templated with 16R5, 8R5, and 4R5 yielded NPNs, nano-

particles and nanoribbons, and nanoparticles and NPNs, respectively. At Pd90, the R5 peptide produces only nanoribbons,^{38–40} yet the 8R5 and 4R5 templates yielded multiple morphologies. Similarly, NPNs are formed at a Pd:R5 ratio of 120 for the R5 only scaffold,^{38–40} while most of the peptide/dendrimer complexes are unable to form stable nanomaterials at this ratio. Moreover, the clear transition between the different morphologies at increasing Pd concentrations is not as defined when using peptide/dendrimer conjugates. Such instances were clearly observed in the majority of the R5/PAMAM systems as the examined ratios displayed multiple morphologies. This nanomorphology effect can likely be attributed to the dendrimer within the bioscaffold, resulting in significant structural and template modulations, as depicted in Scheme 1. To this end, the bioframework is formed via random assembly of the peptide-dendrimer conjugates. Upon reduction of the Pd²⁺ ions sequestered within the structure, spherical nanoparticles are initially formed. To generate the nanoribbons and NPNs, linear particle aggregation must occur. In the R5 only template, the peptide strands guide linear nanoparticle aggregation; however, such a process is likely to be

impeded by the dendrimers integrated into the present templates, where the large organic macromolecules should sterically prevent two Pd particles from interacting across the polymeric component. As such, linear particle aggregation and morphology formation is obstructed, resulting in multiple Pd morphologies in a single sample. Such an event is in direct contrast to the R5 only template where the dendrimers are not present, resulting in a more morphologically homogeneous sample set. Moreover, the lysine groups of the peptide on the dendrimer periphery have a higher affinity for Pd than the tertiary amines within the interior of the polymer. Such a bias results in a template wherein a fraction of the total organic material is unavailable to interact with the metal component, effectively reducing the metal loading capacity of the template. As a consequence, anisotropic morphologies tend to occur at lower Pd:R5 ratios compared to the R5-only scaffold.

It is also worth mentioning that the formation of Pd dendrimer-encapsulated nanoparticles (DENs) is unlikely using these templates. Previous reports of Pd DENs demonstrated the production of uniform particles that are much smaller in size (1.2–1.5 nm) compared to materials templated by the R5-dendrimer conjugates.^{59–61} Such size scales are largely absent from the size histograms obtained from TEM analysis (Supporting Information, Figure S1). Moreover, the amount of Pd per conjugate is substantially greater than what could be loaded into the G4 PAMAM–OH dendrimer hosts,^{45,62} which would lead to Pd precipitation in the absence of the surface-constrained peptides. Finally, the primary amines of the peptide also possess stronger interactions with the Pd²⁺ metal ions compared to the interior tertiary amines of the dendrimer, thus inhibiting metal uptake into the polymer to prevent DEN formation. Taken together, this suggests that attachment of the biomolecules to the dendrimer controls the metallic morphology based upon template effects, which are controlled by the number and structure of surface bound peptides.

Once the nanomaterials were characterized, their catalytic properties were tested using the hydrogenation of allyl alcohol to 1-propanol (Figure 3a). Hydrogenation reactions are critically important on industrial scales,⁶³ where the peptide-dendrimer conjugate template could directly influence the material properties. To this end, the presence of dendrimers within the R5 template may perturb the scaffold, making it more porous for enhanced substrate diffusion to the reactive metal surface. This, in turn, would likely lead to higher degrees of reactivity. For this reaction, 0.05 mol % Pd of each material was bubbled with H₂ for 30 min in H₂O at room temperature to saturate the metallic surface with H₂. Following the addition of the allyl alcohol substrate, hydrogenation of the olefin to 1-propanol occurred at the metallic surface. Formation of propionaldehyde, an allyl alcohol isomer, was also observed in minor amounts during the initial stages of the reaction, where the isomer was eventually converted to the anticipated final product.

To quantify the reaction efficiency, aliquots were extracted at selected time intervals to determine TOF values for each system. The reaction TOFs for the dendrimer/R5-templated Pd nanomaterials are shown in Figure 3b and Table 1. In general, the catalytic reactivities of the materials prepared at different Pd:peptide ratios were quite similar, with average TOFs ranging between ~4000 and 4800 mol product (mol Pd × h)⁻¹. Such values are significantly higher than those obtained from the Pd materials templated by the free R5 peptide template, which possessed an average TOF of 3000 ± 100 mol

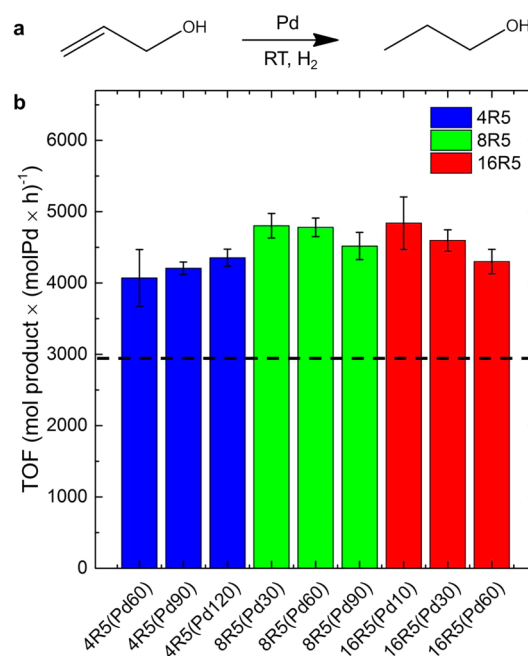


Figure 3. Catalytic analysis of the R5/dendrimer templated Pd nanomaterials: (a) the reaction scheme and (b) TOF values for the hydrogenation of allyl alcohol. The black dashed line represents the average TOF value for Pd nanomaterials templated with free R5 at ratios of 60–120 incremented by 10.⁴⁰

product (mol Pd × h)⁻¹ across all Pd:R5 ratios, as previously reported.⁴⁰ This average is represented by the dashed line in Figure 3b for a direct comparison. To the best of our knowledge, these TOFs represent some of the highest values reported for the hydrogenation of allyl alcohol using comparable Pd nanocatalysts.^{40,64–68} In particular, Pd DENs created inside G4-PAMAM dendrimers yielded a TOF of 480 mol product (mol Pd × h)⁻¹ for the hydrogenation of allyl alcohol, which is significantly lower than the values obtained for the materials prepared using the R5/PAMAM conjugates.⁶⁷ Note that when the hydrogenation of allyl alcohol was studied in the presence of the metal free dendrimer, R5 peptide, and R5/dendrimer conjugates, no product formation or substrate isomerization was observed.

While it is clear that significantly enhanced reactivity was observed from the Pd nanomaterials templated with the R5/dendrimer conjugates compared to their R5 only templated counterparts, the metallic structures of both sets of materials were similar in size, composition, and morphology as examined by TEM. As such, the R5/dendrimer conjugate may promote enhanced reactivity by altering the spatial arrangement of Pd nanomaterials through changes in the template organic framework. To probe these structural features, DLS and SAXS studies were performed to provide size-scale structural information on the Pd nanomaterials templated by both free and dendrimer-bound R5 scaffolds. From this data, comparative analysis of the global structural differences can be determined in solution, including both the organic and inorganic, which is difficult to assess using microscopy methods that typically require a sample in the solid state. DLS data for Pd nanomaterials templated with the R5-PAMAM conjugates demonstrated size aggregates in solution ranging from 150 to 350 nm (Figure 4a). Such a size range is nearly 100-fold larger than the inorganic components observed by TEM. Note this is

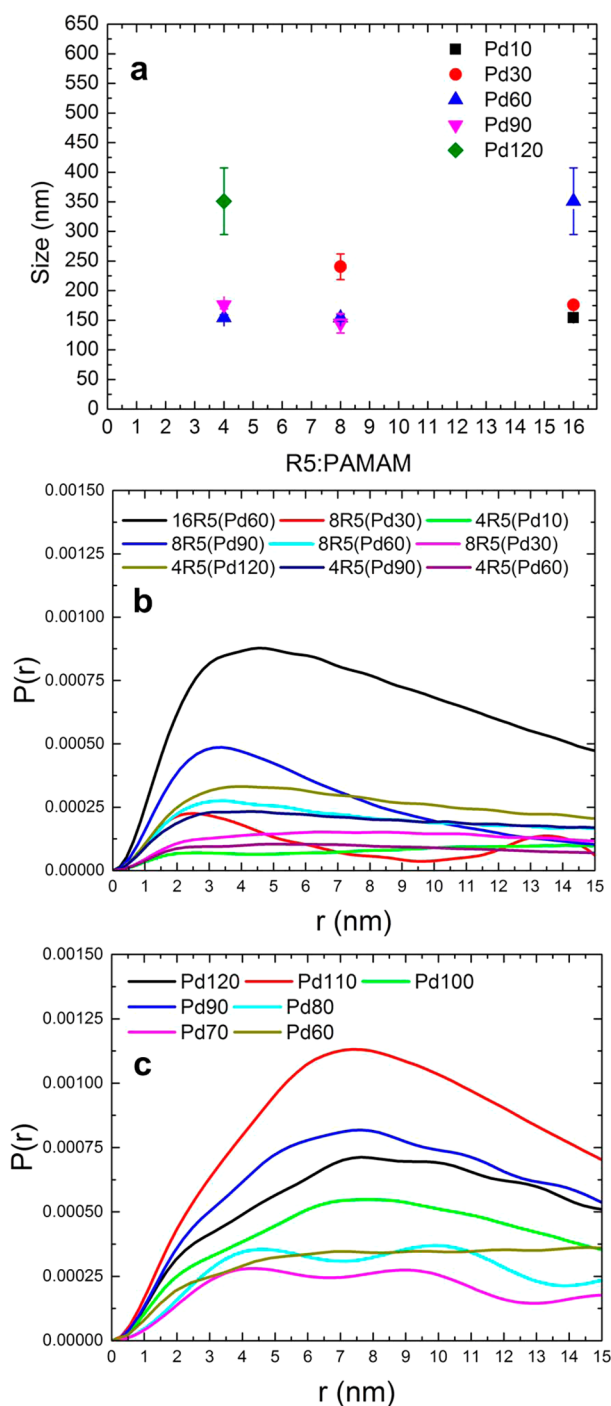


Figure 4. (a) DLS of Pd nanomaterials templated with the R5/dendrimer bioconjugate and PDDFs of the Pd nanomaterials templated with (b) the R5/dendrimer scaffold and (c) the unconstrained R5 framework.

a similar aggregate size range for the Pd structures templated with free R5 over a series of Pd:R5 ratios.⁴⁰ Given the observation achieved via TEM for the metallic component, the overall larger structures measured via DLS, which represent the entire templated structure including the bioframework, are presumed to be semihollow, allowing for relatively easy substrate diffusion, catalytic turnover, and product release. This semihollow structure correlates well with the materials growing within the biomimetic framework that is not completely filled by the metallic components. Should the

scaffolds be completely filled, significantly larger and randomly aggregated bulk Pd would have been observed by TEM, which was never observed for any of the samples.

To more fully evaluate the global structure of the biotemplated materials, SAXS analysis was completed. SAXS patterns (Supporting Information, Figure S2) were obtained for the Pd nanostructures templated by both the R5/PAMAM and unconstrained R5 frameworks. Due to the various morphologies obtained via these approaches (particularly those samples containing anisotropic particles and/or a mixture of morphologies), simple analysis of the Guinier and Porod regions of the SAXS pattern could not be achieved. Pair-distance distribution function (PDDF) analysis, however, can be used on the obtained SAXS patterns for materials displaying a higher degree of inhomogeneity and comparative irregularity. In this method, the SAXS pattern is fit to an autocorrelation function and inverse Fourier transformed into real-space distances. The resulting PDDF, $P(r)$, describes the distances between scattering objects (i.e., Pd atoms) in a larger macromolecular structure.⁶⁹ As shown in Figure 4b, PDDFs for the Pd nanostructures templated by the R5/PAMAM conjugates exhibited maximums of ~ 3 nm for all samples and then extended to larger pair distances. This particle size is consistent with the size-scales observed for the metallic components by TEM, an indication that the minimum possible size for Pd is obtained in solution using R5/dendrimer templates and local particle aggregation is avoided. Conversely, the Pd materials templated by the free R5 scaffold possessed markedly different PDDFs, where the maximums were between 6 and 10 nm for all Pd:R5 ratios (Figure 4c). Such an increase in the first pair distances suggests that differing degrees of local particle aggregation occurred using the unconstrained peptide template. Note that lower pair-distance shoulders are present for Pd templated with unconstrained R5, indicating a degree of nonaggregated nanomaterials in solution. The highly flexible R5 scaffolds can more easily participate in intermolecular interactions compared to the conformationally hindered peptides in the dendrimer conjugates. Such increases in template–template interactions likely facilitates an enhanced Pd aggregation as observed in the PDDF data for R5-templated Pd.

It is worth noting that the PDDFs were extended to larger sizes (Supporting Information, Figure S3), which indicated that larger Pd superstructures were assembled, consistent with DLS data (Figure 4a). Under these considerations and the observations from the SAXS and DLS data, the availability of the reactive Pd surface within the template is higher for materials generated with R5–dendrimer conjugates. In contrast, the aggregated Pd structures found within the R5 template were likely to impede substrate diffusion and present a lower metallic surface area, thus diminishing the catalytic reactivity for the hydrogenation of allyl alcohol as compared to R5–dendrimer templated materials.

CONCLUSIONS

In summary, PAMAM dendrimers were used as water-soluble scaffolds for the attachment of R5 peptides, which together mimic materials-binding peptide architectures found in nature. These R5–dendrimer conjugates were capable of templating Pd nanomaterials of varying morphologies, whose structures were dependent on the Pd:R5 ratio and peptide surface density on the dendrimer periphery. Furthermore, morphological trends from R5/dendrimer-templated Pd nanomaterials differ

from those created using the free R5 scaffold in solution, indicating that the conformation of the peptide sequence and the incorporated polymer component are critically important in dictating both the Pd morphology and catalytic activity. Once generated, the reactivity was probed using the hydrogenation of allyl alcohol as a model system. For this, the majority of the Pd materials templated with the peptide/dendrimer constructs demonstrated TOFs of >1000 mol product $(\text{mol Pd} \times \text{h})^{-1}$ units higher than the materials generated using the dendrimer-free peptide templates. Similarities in particle size observed from TEM indicated that the increase in catalytic activity was due to differences in the arrangement of both the templates and the Pd materials, which was confirmed via SAXS and DLS. PDDF analysis from the SAXS patterns showed that the R5-dendrimer-templated Pd displayed size-scales consistent with TEM observations, while the free R5-templated materials tended to aggregate into larger structures, effectively reducing the available surface area for catalysis. More generally, this study demonstrates the capability to alter the morphology and properties of peptide-derived nanomaterials by simply choosing a system that mimics the constrained nature of the material binding peptide observed in nature.

METHODS

Materials. Hydroxyl-terminated G4 PAMAM (ethylenediamine core), K_2PdCl_4 , NaBH_4 , allyl alcohol, and antifoam SE-15 (nonionic 10% emulsion of silicone defoamer) were purchased from Sigma. *N*-(*p*-maleimidophenyl)isocyanate was purchased from Thermo Scientific, while dimethyl sulfoxide (DMSO) was purchased from BDH Chemicals. All Fmoc amino acids and chemicals used in peptide synthesis were purchased from Advanced Chemtech. Ultrapure, 18.2 M Ω cm water was used for all experiments.

R5/Dendrimer Conjugation. All peptides were synthesized using standard solid-phase Fmoc automated peptide synthesis protocols employing a TETRAS model peptide synthesizer (CreoSalus).⁷⁰ Once prepared, the crude peptides were purified via reverse-phase HPLC and confirmed by MALDI TOF mass spectrometry. Cysteine-labeled R5 peptides were covalently attached to the surface of hydroxyl-terminated G4 PAMAM dendrimers using PMPI. For this, an aqueous dendrimer solution was prepared at a concentration of 5 μM and a pH of 9.00–9.25 using KOH to drive the coupling of PMPI to the surface hydroxyls. Fresh PMPI stocks were made at 0.1 M in DMSO and added to the PAMAM solutions at the desired stoichiometric ratio for peptide coupling. Ratios of 4, 8, and 16 peptides per dendrimer were studied. PMPI coupling to the dendrimer was performed under magnetic stirring for at least 2.0 h at room temperature. Once the PMPI was coupled to the dendrimer surface, the materials were dialyzed using SnakeSkin dialysis tubing (7000 MWCO) for at least 5.0 h to remove any unreacted coupling reagent. Subsequently, the pH of the PMPI-modified dendrimers was adjusted to 6.25–6.75 using HCl, after which stoichiometric amounts of the cysteine-containing peptides were added from a freshly prepared 10 mg/mL peptide stock solution. After at least 2.0 h of reaction while vigorously stirring, the R5-dendrimer conjugates were dialyzed for ≥ 12.0 h to remove any unreacted peptide.

Pd Nanomaterial Synthesis. The Pd nanomaterials encapsulated within the peptide/dendrimer template were synthesized at specific metal:peptide ratios using previously described methods.^{38–41} Briefly, 400 μL of 5 μM R5/dendrimer conjugate was added to a predetermined volume of H_2O such that the final conjugate concentration was 1 μM . Under magnetic stirring, freshly prepared, aqueous 0.1 M K_2PdCl_4 was added at selected Pd:peptide ratios. Note that Pd:peptide ratios were used and not Pd:dendrimer ratios. After 15 min of stirring, 75 μL of freshly prepared 0.1 M NaBH_4 was added to reduce the Pd^{2+} to Pd. Nanomaterial samples that were not stable after 24 h were not used for characterization or catalytic analysis.

Allyl Alcohol Hydrogenation. Catalytic hydrogenation of allyl alcohol with the Pd nanoparticles was performed using previously published methods.^{40,64} Briefly, 0.05 mol % Pd of the different materials was added to 25.0 mL of H_2O and 20.0 μL of antifoam in a three-neck round-bottom flask. Under constant stirring, H_2 gas was bubbled through the solution using a glass gas dispersion tube at a gauge pressure of 50 kPa. After 30 min, 25.0 mL of a 50.0 mM aqueous allyl alcohol solution was added to the reaction flask, followed immediately by the removal of a 1.00 mL aliquot to serve as an initial time point. Subsequent aliquots were extracted at 1, 5, 10, 15, 20, 25, and 30 min. The extracted aliquots were injected into a gas chromatograph (GC—Agilent 7820A) equipped with a DB-ALC1 column and a flame ionization detector (FID) without further purification. GC response factors were determined using standard solutions of allyl alcohol, *n*-propanol (product), and propionaldehyde (isomer).⁶⁴ With retention times and response factors established, TOF values were calculated.

Characterization. The formation of the R5-dendrimer conjugates was confirmed using attenuated total reflectance Fourier transform infrared spectroscopy (ATR-FTIR, PerkinElmer Frontier) by analyzing solid samples produced via lyophilization of aqueous solutions (Labconco, FreeZone 4.5). Comparison of the number of covalently attached peptides to each PAMAM dendrimer was accomplished via fluorescence measurements employing tryptophan as a fluorescent label. Using the automated peptide synthesis techniques described above, the fluorescent residue was incorporated at the opposite termini of the cysteine moiety. The fluorescence was measured with a $\lambda_{\text{ex}} = 280$ nm and a $\lambda_{\text{em}} = 348$ nm using a BioTek Synergy H1 Hybrid Multi-Mode Microplate Reader. CD spectroscopy was performed on a Jasco J-815 CD spectrometer using a quartz cuvette with a 0.5 cm path length from 190–300 nm at a scan rate of 20 nm/min. The peptide concentration (not conjugate concentration) in solution was 50 μM . Secondary structure contributions were deconvoluted from the individual CD spectrum using CDPro software. DLS studies were conducted using a Malvern Zetasizer nano ZS instrument. TEM analysis of the Pd nanomaterial morphologies was examined using a Phillips CM-200, while HRTEM was performed on a FEI Titan. Sizing analysis was performed on at least five individual images using >100 different structures to complete the histograms. The relative morphology population created per peptide-dendrimer conjugate was determined by counting the number of structures in at least five individual images. SAXS studies were performed at the 12-ID-B beamline at the Advanced Photon Source (APS), Argonne National Laboratory (ANL) using 12 keV irradiation and Pilatus area detector. Samples were analyzed in 2 mm (outer diameter) quartz capillaries at concentrations employed for sample preparation. PDDFs were calculated with the autocorrelation method of Moore⁷¹ using the Irena SAXS data analysis macros written in Igor Pro.⁷²

ASSOCIATED CONTENT

Supporting Information

A detailed schematic of R5-PAMAM conjugation, summaries of R5 secondary structure for R5/PAMAM and CR5, size histograms of Pd nanomaterials from TEM analysis, SAXS patterns of Pd templated with R5-PAMAM and unconstrained R5, and PDDFs derived from SAXS patterns for Pd nanomaterials templated with free R5 and R5/dendrimer conjugates examined at larger pair distances. This material is available free of charge via the Internet at <http://pubs.acs.org>.

AUTHOR INFORMATION

Corresponding Authors

*M.R.K.: Phone (305) 284-9351; e-mail knecht@miami.edu.

*R.R.N.: Phone (937) 255-9717; e-mail rajesh.naik@us.af.mil.

Present Address

^{||}R.B.: Department of Chemical and Materials Engineering, University of Kentucky, Lexington, Kentucky 40506, United States.

Funding

This work was supported in part by the Air Force Office of Scientific Research (RN) and National Science Foundation (M.R.K.: DMR-1145175). Further financial support was provided by University of Miami. N.M.B acknowledges fellowship support from the National Research Council Research Associateship award. Use of the Advanced Photon Source, an Office of Science User Facility operated for the U.S. Department of Energy (DOE) Office of Science by Argonne National Laboratory, was supported by the U.S. DOE under Contract No. DE-AC02-06CH11357.

Notes

The authors declare no competing financial interest.

ACKNOWLEDGMENTS

The authors acknowledge Ms. Beverley Briggs for assistance with peptide synthesis.

REFERENCES

- (1) Dickerson, M. B.; Sandhage, K. H.; Naik, R. R. *Chem. Rev.* **2008**, *108*, 4935–4978.
- (2) Sarikaya, M.; Tamerler, C.; Jen, A. K. Y.; Schulten, K.; Baneyx, F. *Nat. Mater.* **2003**, *2*, 577–585.
- (3) Briggs, B. D.; Knecht, M. R. *J. Phys. Chem. Lett.* **2012**, *3*, 405–418.
- (4) Brown, S. *Nat. Biotechnol.* **1997**, *15*, 269–272.
- (5) Naik, R. R.; Stringer, S. J.; Agarwal, G.; Jones, S. E.; Stone, M. O. *Nat. Mater.* **2002**, *1*, 169–172.
- (6) Chiu, C.-Y.; Li, Y.; Ruan, L.; Ye, X.; Murray, C. B.; Huang, Y. *Nat. Chem.* **2011**, *3*, 393–399.
- (7) Pacardo, D. B.; Sethi, M.; Jones, S. E.; Naik, R. R.; Knecht, M. R. *ACS Nano* **2009**, *3*, 1288–1296.
- (8) Reiss, B. D.; Mao, C.; Solis, D. J.; Ryan, K. S.; Thomson, T.; Belcher, A. M. *Nano Lett.* **2004**, *4*, 1127–1132.
- (9) Patwardhan, S. V.; Emami, F. S.; Berry, R. J.; Jones, S. E.; Naik, R. R.; Deschaume, O.; Heinz, H.; Perry, C. C. *J. Am. Chem. Soc.* **2012**, *134*, 6244–6256.
- (10) Dickerson, M. B.; Jones, S. E.; Cai, Y.; Ahmad, G.; Naik, R. R.; Kröger, N.; Sandhage, K. H. *Chem. Mater.* **2008**, *20*, 1578–1584.
- (11) Ahmad, G.; Dickerson, M. B.; Cai, Y.; Jones, S. E.; Ernst, E. M.; Vernon, J. P.; Haluska, M. S.; Fang, Y.; Wang, J.; Subramanyam, G.; Naik, R. R.; Sandhage, K. H. *J. Am. Chem. Soc.* **2007**, *130*, 4–5.
- (12) Arakaki, A.; Webb, J.; Matsunaga, T. *J. Biol. Chem.* **2003**, *278*, 8745–8750.
- (13) Thai, C. K.; Dai, H.; Sastry, M. S. R.; Sarikaya, M.; Schwartz, D. T.; Baneyx, F. *Biotechnol. Bioeng.* **2004**, *87*, 129–137.
- (14) Flynn, C. E.; Mao, C.; Hayhurst, A.; Williams, J. L.; Georgiou, G.; Iverson, B.; Belcher, A. M. *J. Mater. Chem.* **2003**, *13*, 2414–2421.
- (15) Whaley, S. R.; English, D. S.; Hu, E. L.; Barbara, P. F.; Belcher, A. M. *Nature* **2000**, *405*, 665–668.
- (16) Mao, C.; Flynn, C. E.; Hayhurst, A.; Sweeney, R.; Qi, J.; Georgiou, G.; Iverson, B.; Belcher, A. M. *Proc. Nat. Acad. Sci. U.S.A.* **2003**, *100*, 6946–6951.
- (17) Spoerke, E. D.; Voigt, J. A. *Adv. Funct. Mater.* **2007**, *17*, 2031–2037.
- (18) Wang, S.; Humphreys, E. S.; Chung, S.-Y.; Delduco, D. F.; Lustig, S. R.; Wang, H.; Parker, K. N.; Rizzo, N. W.; Subramoney, S.; Chiang, Y.-M.; Jagota, A. *Nat. Mater.* **2003**, *2*, 196–200.
- (19) Cui, Y.; Kim, S. N.; Jones, S. E.; Wissler, L. L.; Naik, R. R.; McAlpine, M. C. *Nano Lett.* **2010**, *10*, 4559–4565.

- (20) Kim, S. N.; Kuang, Z.; Slocik, J. M.; Jones, S. E.; Cui, Y.; Farmer, B. L.; McAlpine, M. C.; Naik, R. R. *J. Am. Chem. Soc.* **2011**, *133*, 14480–14483.
- (21) So, C. R.; Hayamizu, Y.; Yazici, H.; Gresswell, C.; Khatayevich, D.; Tamerler, C.; Sarikaya, M. *ACS Nano* **2012**, *6*, 1648–1656.
- (22) Tang, Z.; Palafox-Hernandez, J. P.; Law, W.-C.; E. Hughes, Z.; Swihart, M. T.; Prasad, P. N.; Knecht, M. R.; Walsh, T. R. *ACS Nano* **2013**, *7*, 9632–9646.
- (23) Slocik, J. M.; Naik, R. R. *Adv. Mater.* **2006**, *18*, 1988–1992.
- (24) Nam, K. T.; Kim, D.-W.; Yoo, P. J.; Chiang, C.-Y.; Meethong, N.; Hammond, P. T.; Chiang, Y.-M.; Belcher, A. M. *Science* **2006**, *312*, 885–888.
- (25) Kuang, Z.; Kim, S. N.; Crookes-Goodson, W. J.; Farmer, B. L.; Naik, R. R. *ACS Nano* **2009**, *4*, 452–458.
- (26) Slocik, J. M.; Tam, F.; Halas, N. J.; Naik, R. R. *Nano Lett.* **2007**, *7*, 1054–1058.
- (27) Lee, Y. J.; Lee, Y.; Oh, D.; Chen, T.; Ceder, G.; Belcher, A. M. *Nano Lett.* **2010**, *10*, 2433–2440.
- (28) Nam, Y. S.; Park, H.; Magyar, A. P.; Yun, D. S.; Pollom, T. S.; Belcher, A. M. *Nanoscale* **2012**, *4*, 3405–3409.
- (29) Cui, Y.; Kim, S. N.; Naik, R. R.; McAlpine, M. C. *Acc. Chem. Res.* **2012**, *45*, 696–704.
- (30) Slocik, J. M.; Zabinski, J. S.; Phillips, D. M.; Naik, R. R. *Small* **2008**, *4*, 548–551.
- (31) Coppage, R.; Slocik, J. M.; Sethi, M.; Pacardo, D. B.; Naik, R. R.; Knecht, M. R. *Angew. Chem., Int. Ed.* **2010**, *49*, 3767–3770.
- (32) Coppage, R.; Slocik, J. M.; Ramezani-Dakheel, H.; Bedford, N. M.; Heinz, H.; Naik, R. R.; Knecht, M. R. *J. Am. Chem. Soc.* **2013**, *135*, 11048–11054.
- (33) Kröger, N.; Deutzmann, R.; Sumper, M. *Science* **1999**, *286*, 1129–1132.
- (34) Chen, C.-L.; Zhang, P.; Rosi, N. L. *J. Am. Chem. Soc.* **2008**, *130*, 13555–13557.
- (35) Sewell, S. L.; Wright, D. W. *Chem. Mater.* **2006**, *18*, 3108–3113.
- (36) Cole, K. E.; Ortiz, A. N.; Schoonen, M. A.; Valentine, A. M. *Chem. Mater.* **2006**, *18*, 4592–4599.
- (37) Bhandari, R.; Knecht, M. R. *Catal. Sci. Technol.* **2012**, *2*, 1360–1366.
- (38) Jakhmola, A.; Bhandari, R.; Pacardo, D. B.; Knecht, M. R. *J. Mater. Chem.* **2010**, *20*, 1522–1531.
- (39) Bhandari, R.; Knecht, M. R. *ACS Catal.* **2011**, *1*, 89–98.
- (40) Bhandari, R.; Pacardo, D. B.; Bedford, N. M.; Naik, R. R.; Knecht, M. R. *J. Phys. Chem. C* **2013**, *117*, 18053–18062.
- (41) Bhandari, R.; Knecht, M. R. *Langmuir* **2012**, *28*, 8110–8119.
- (42) Grayson, S. M.; Fréchet, J. M. J. *Chem. Rev.* **2001**, *101*, 3819–3868.
- (43) Crooks, R. M.; Zhao, M.; Sun, L.; Chechik, V.; Yeung, L. K. *Acc. Chem. Res.* **2000**, *34*, 181–190.
- (44) Myers, V. S.; Weir, M. G.; Carino, E. V.; Yancey, D. F.; Pande, S.; Crooks, R. M. *Chem. Sci.* **2011**, *2*, 1632–1646.
- (45) Bronstein, L. M.; Shifrina, Z. B. *Chem. Rev.* **2011**, *111*, 5301–5344.
- (46) Esfand, R.; Tomalia, D. A. *Drug Discovery Today* **2001**, *6*, 427–436.
- (47) Mintzer, M. A.; Grinstaff, M. W. *Chem. Soc. Rev.* **2011**, *40*, 173–190.
- (48) Stiriba, S.-E.; Frey, H.; Haag, R. *Angew. Chem., Int. Ed.* **2002**, *41*, 1329–1334.
- (49) Barth, A. *Prog. Biophys. Mol. Biol.* **2000**, *74*, 141–173.
- (50) Jackson, M.; Mantsch, H. H. *Crit. Rev. Biochem. Mol. Biol.* **1995**, *30*, 95–120.
- (51) Wood, R.; Piantadosi, C.; Snyder, F. J. *Lipid Res.* **1969**, *10*, 370–373.
- (52) Pender, M. J.; Sowards, L. A.; Hartgerink, J. D.; Stone, M. O.; Naik, R. R. *Nano Lett.* **2005**, *6*, 40–44.
- (53) Nygren, P.; Lundqvist, M.; Broo, K.; Jonsson, B.-H. *Nano Lett.* **2008**, *8*, 1844–1852.
- (54) Doi, N.; Yanagawa, H. *Cell. Mol. Life Sci.* **1998**, *54*, 394–404.

- (55) Higashi, N.; Koga, T.; Niwa, M. *ChemBioChem* **2002**, *3*, 448–454.
- (56) Javor, S.; Natalello, A.; Doglia, S. M.; Reymond, J.-L. *J. Am. Chem. Soc.* **2008**, *130*, 17248–17249.
- (57) Örbeg, M.-L.; Schillén, K.; Nylander, T. *Biomacromolecules* **2007**, *8*, 1557–1563.
- (58) Knecht, M. R.; Wright, D. W. *Chem. Commun.* **2003**, 3038–3039.
- (59) Zhao, M.; Crooks, R. M. *Angew. Chem., Int. Ed.* **1999**, *38*, 364–366.
- (60) Wilson, O. M.; Knecht, M. R.; Garcia-Martinez, J. C.; Crooks, R. M. *J. Am. Chem. Soc.* **2006**, *128*, 4510–4511.
- (61) Pande, S.; Weir, M. G.; Zaccaro, B. A.; Crooks, R. M. *New J. Chem.* **2011**, *35*, 2054–2060.
- (62) Scott, R. W. J.; Ye, H.; Henriquez, R. R.; Crooks, R. M. *Chem. Mater.* **2003**, *15*, 3873–3878.
- (63) Murphree, E. V.; Brown, C. L.; Gohr, E. J. *Ind. Eng. Chem.* **1940**, *32*, 1203–1212.
- (64) Bhattacharjee, S.; Bruening, M. L. *Langmuir* **2008**, *24*, 2916–2920.
- (65) Jiang, Y.; Gao, Q. *J. Am. Chem. Soc.* **2005**, *128*, 716–717.
- (66) Oh, S.-K.; Niu, Y.; Crooks, R. M. *Langmuir* **2005**, *21*, 10209–10213.
- (67) Niu, Y.; Yeung, L. K.; Crooks, R. M. *J. Am. Chem. Soc.* **2001**, *123*, 6840–6846.
- (68) Ornelas, C.; Ruiz, J.; Salmon, L.; Astruc, D. *Adv. Synth. Catal.* **2008**, *350*, 837–845.
- (69) Hong, X.; Hao, Q. *Appl. Phys. Lett.* **2009**, *94*, 083903–083903–3.
- (70) Chan, W. C.; White, P. D. *Fmoc Solid Phase Peptide Synthesis*; Oxford University Press: Oxford, 2004.
- (71) Moore, P. J. *Appl. Crystallogr.* **1980**, *13*, 168–175.
- (72) Ilavsky, J.; Jemian, P. R. *J. Appl. Crystallogr.* **2009**, *42*, 347–353.